

Simulation and Measurement of Stray Fields for the Manipulation of Spin Qubits in One- and Two-Dimensional Arrays

Michele Aldeghi, Rolf Allenspach, Andriani Vervelaki, Daniel Jetter, Kousik Bagani, Floris Braakman, Martino Poggio, and Gian Salis*



Cite This: *Nano Lett.* 2025, 25, 1838–1844



Read Online

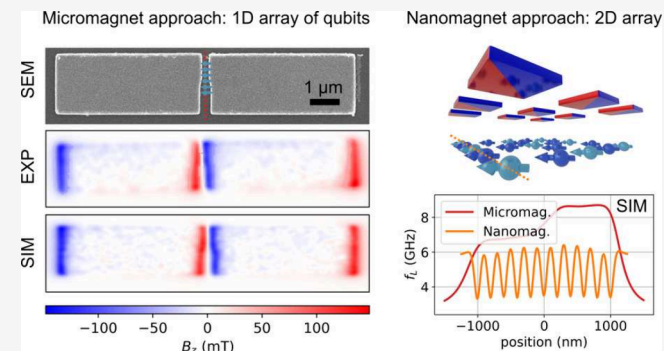
ACCESS |

Metrics & More

Article Recommendations

Supporting Information

ABSTRACT: The inhomogeneous magnetic stray field of micromagnets has been extensively used to manipulate electron spin qubits. By means of micromagnetic simulations and scanning superconducting quantum interference device microscopy, we show that the polycrystallinity of the magnet and nonuniform magnetization significantly impact the stray field and corresponding qubit properties. The random orientation of the crystal axis in polycrystalline Co magnets alters the qubit frequencies by up to 0.5 GHz, compromising single qubit addressability and single gate fidelities. We map the stray field of Fe micromagnets with an applied magnetic field of up to 500 mT, finding field gradients above 1 mT/nm. The measured gradients and the lower magnetocrystalline anisotropy of Fe demonstrate the advantage of using Fe instead of Co as magnets in spin qubit devices. These



properties of Fe also enabled us to design a 2D arrangement of

KEYWORDS: nanomagnets, spin qubits, electric dipole spin resonance, scanning SQUID microscopy

Engineering the stray field profile of magnets at the nanoscale finds widespread applications, ranging from technological applications for magnetic storage¹ and sensing² to studying complex phenomena like phase transitions³ and nanoscale imaging.⁴ One application that requires exquisite control of the stray field of nanomagnets is quantum computation with electron spins. There, spins of electrons electrostatically confined in quantum dots⁵ define qubits that can be manipulated via electric dipole spin resonance (EDSR),^{6–8} in which the electron's wave function is resonantly displaced within the inhomogeneous stray field of a micromagnet. Single-qubit gate fidelities of 99.9%⁹ and control of up to six qubits¹⁰ were achieved, with two-qubit gates fidelity reaching up to 99.8%.^{11–13}

Qubit gate fidelity and addressability depend on the interplay between the electron confinement (controlled by electric fields) and the local magnetic field profile given by the magnet. The shape of the magnet needs to be adapted to the device-specific qubit arrangement and number,¹⁴ with the goal to maximize qubit gate fidelity while providing addressability of individual qubits. Gradients of field components transversal to the main field direction are used for Rabi driving of the qubits by an AC electric field, while longitudinal gradients spectrally separate neighboring qubits to enable individual addressability. However, in combination with charge noise, the longitudinal field gradient is the main responsible source for qubit

dephasing,¹⁵ dominant over the effect of magnetic fluctuations at finite temperatures.¹⁶ Making informed decisions about the design of the magnet therefore requires an exact knowledge of the stray field profile.

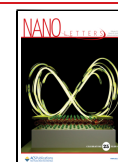
This Letter shows that nonuniform magnetization, polycrystallinity, and fabrication imperfections of the lithographically defined magnets affect qubit properties to a much larger extent than previously assumed. We measure the stray field of Fe magnets by scanning superconducting quantum interference device (SQUID) microscopy (SSM)¹⁷ and compare it with micromagnetic simulations, disentangling the effects of polycrystallinity, surface roughness, and reduced saturation magnetization. We then apply our model to a spin qubit experiment with the same magnet design,¹⁰ showing that spin qubit properties can be accurately modeled. Finally, we propose a magnet geometry resilient to polycrystallinity-induced stray field variations that enables the manipulation of spin qubits arranged on a two-dimensional lattice.

Received: October 14, 2024

Revised: January 8, 2025

Accepted: January 9, 2025

Published: January 22, 2025



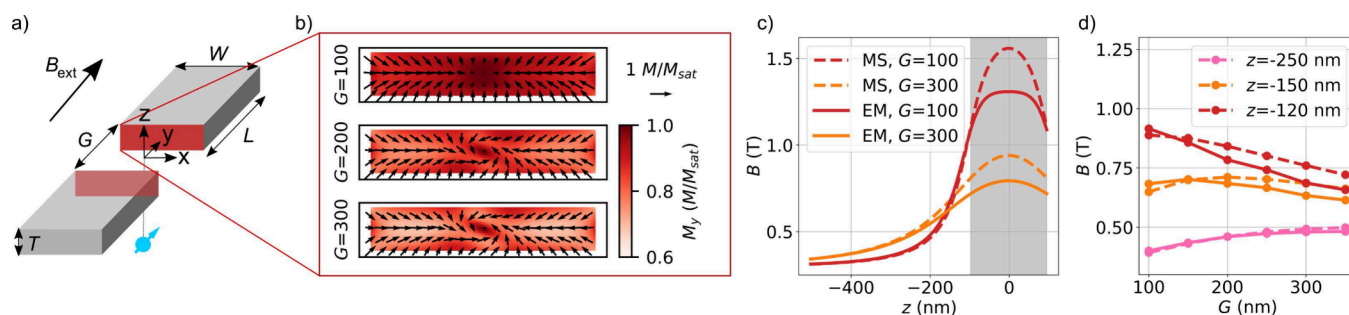


Figure 1. Comparison of magnetization pattern and magnetic field (B) between the MS approximation and EM micromagnetic simulations. (a) Device geometry, showing magnets (gray), qubit (blue spins), and B_{ext} . The origin of the coordinate system is centered in the middle of the gap. (b) The magnetization pattern (EM simulations) at the surface of the magnet depends on the gap distance G (given in nm) with $B_{\text{ext}} = 0.3$ T. In-plane components are shown as arrows, the out-of-plane component as color. The length of the arrow above the color scale corresponds to saturation magnetization. (c, d) Stray field magnitude for different height and gap distances (continuous lines: EM, dashed lines: MS). The gray shaded area in (c) shows the z position of the magnets.

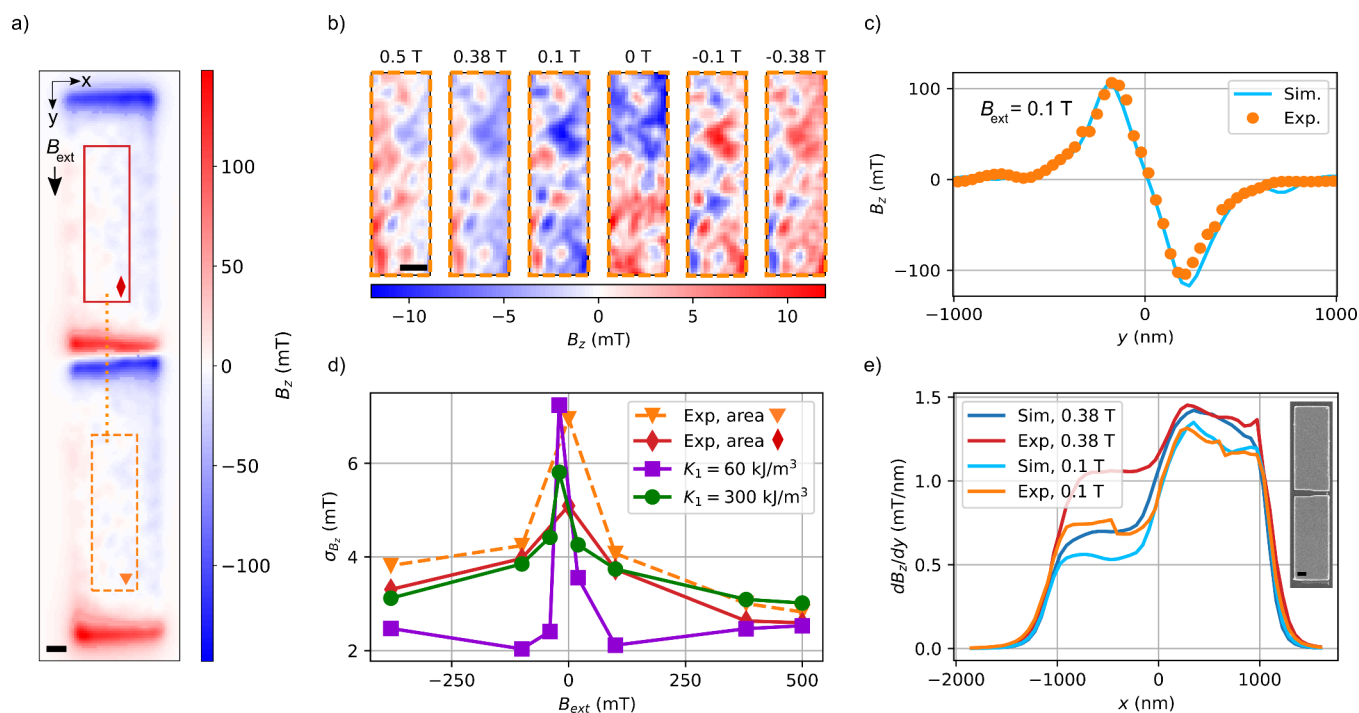


Figure 2. SSM measurements and simulations of the stray field at $z = 70$ nm (where $z = 0$ is at the upper surface of the magnets). (a) B_z stray field SSM measurements for $B_{\text{ext}} = 0.1$ T. (b) Magnification of the area framed by the orange dashed line in (a) for different B_{ext} . (c) Measured and simulated B_z , extracted along the orange dotted line in (a). (d) Standard deviation of B_z versus B_{ext} for the regions enclosed by the rectangles in (a). The lines are guides to the eye. (e) Fitted driving gradient dB_z/dy in the middle of the gap ($y = 0$) between the magnets at two B_{ext} . The inset shows a SEM image of the measured device. All scale bars are 500 nm.

Two methods are commonly used to compute the stray field from micromagnets: one based on the macrospin approximation (abbreviated as “MS”) and one where the magnetization pattern is computed by micromagnetic simulations to reach an energy minimum (abbreviated as “EM”). In the MS approach, magnetization within the entire magnet is assumed to be uniform. In the EM approach, a magnetization pattern is calculated by minimizing the overall energy of the system.¹⁸ The total magnetic field B (with $B = B_{\text{ext}} + B_{\text{stray}}$, where B_{ext} is the external magnetic field and B_{stray} is the magnet stray field) is calculated from the magnetization pattern and differs for the two methods such that different qubit properties are predicted. We note that the computationally lighter MS approximation is commonly used for the design of micromagnets for spin qubit,^{8,10,14,19} even though complete magnetic saturation is not

achieved at external magnetic fields usually applied in experiments (ranging from 0.2 to 1 T).

We first show that the MS approximation cannot accurately model the stray field for the manipulation of spin qubits. For this, we illustrate the differences between the MS and the EM results on the simplest magnet geometry useful for EDSR driving, where the opposite poles of two magnets are brought close together [Figure 1(a)], generating a large stray field that can be tuned by changing the gap distance G between the two magnets. In our case, the magnets are cuboids (width $W = 1000$ nm, length $L = 3000$ nm, thickness $T = 200$ nm). We set the origin of the coordinate system in the center of the gap with an external magnetic field $B_{\text{ext}} = 0.3$ T applied along the y direction and the magnets in the x - y plane. The position of the qubits is assumed to be centered in the gap, with an offset

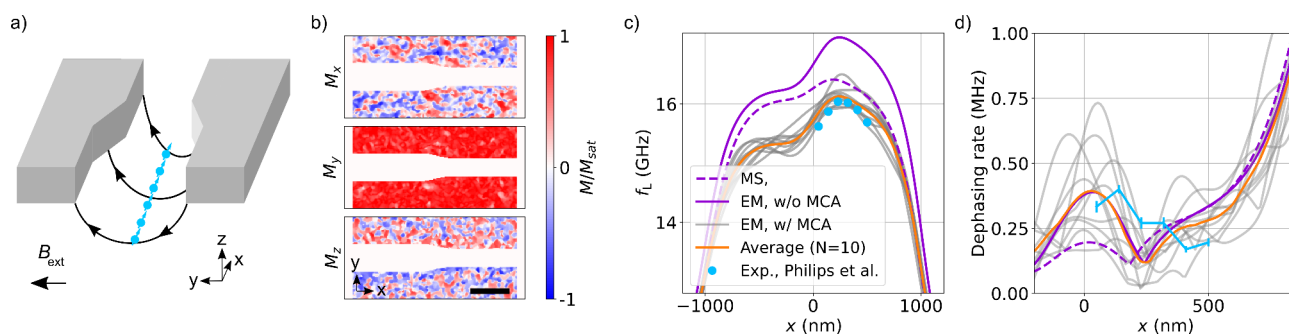


Figure 3. (a) Device geometry. (b) Magnetization pattern of one out of the 10 different crystallite patterns used in the EM simulations at $B_{\text{ext}} = 380$ mT. The scale bar is 500 nm. (c) f_L and (d) dephasing rate profile along the line of qubit for the MS and EM with and without MCA simulations. The 10 different gray lines correspond to 10 different crystallite patterns, and their average is shown in orange. The light blue points in (c) and (d) are the respective values obtained from qubit measurements by Philips et al.¹⁰

in the z direction. In this region, the stray field is mostly set by the magnetization patterns on the two opposing surfaces facing the gap [highlighted in red in Figure 1(a)].

In the MS approximation, the magnetization points perpendicular to these surfaces, creating a large stray field within the volume V_{gap} spanned by the two surfaces. At small fields, such a magnetization pattern costs more magnetostatic energy than what is saved in Zeeman and exchange energy. Shape anisotropy is not sufficient to set a uniform magnetization pattern for these magnets, as the EM simulation predicts a rotation of the magnetization from the out-of-plane toward the in-plane direction at these two surfaces, leading to a stray field reduction. Increasing G leads to more pronounced rotations, due to the reduced magnetostatic interaction between the two magnets [Figure 1(b)].

We compare B obtained from the MS and EM approaches in Figure 1(c), where we focus on profiles along z taken at $x, y = 0$. For both EM and MS simulations, we observe that a larger gap increases B , as shown in Figure 1(d) for $z = -250$ nm, which is a consequence of the dipolar nature of the field distribution close to the gap. The optimal gap size to maximize the stray field therefore depends also on z . The magnetization rotation accounted for in the EM simulation leads to a change of the Larmor frequency $f_L = \frac{g\mu_B}{h}B$ on the order of several GHz if compared to the MS approximation (e.g., for $z = -200$ nm and $G = 300$ nm, the difference is 65 mT, which corresponds to a qubit frequency difference of $\Delta f_L = 1.82$ GHz, with μ_B the Bohr magneton, h Planck's constant, and a g -factor $g = 2$). This is much larger than the typically targeted Δf_L between neighboring qubit frequencies. We note that these differences need to be carefully engineered in a larger array of spin qubits to avoid crosstalk of the EDSR drive with close-by qubits^{14,19} (see also the SI), emphasizing the importance of a precise knowledge of the expected stray field.

Up to here, we have considered ideal magnet geometries with uniform magnetic properties throughout the magnet volume. Now, we take into account lithographically induced modifications of the shape and polycrystalline structure of nanofabricated EDSR magnets. Rounding effects at the edges of the magnet modify the magnetization pattern, with variations of B of up to several GHz (e.g., the Δf_L between a straight and a semicircle profile at $z = -120$ nm is 4.08 GHz; see the SI). Also surface roughness and sample polycrystallinity strongly affect the stray field,²⁰ both of which are typically present in nanofabricated EDSR magnets. Surface roughness varies the stray field through magnetization rearrangement at

the corrugated surface of the magnet and through modulation of the effective distance between the magnet edge and the qubit array. Polycrystallinity further modulates the stray field if the material exhibits a magnetocrystalline anisotropy (MCA), since the magnetization direction will then be different for each crystallite.

We investigate the effect of these nonidealities on B following the design used by Philips et al.¹⁰ [sketched in Figure 3(a)]. E-beam evaporation and lift-off have been used to pattern 100 nm thick Fe magnets capped by 5 nm of Pt on a Si wafer with native oxide [inset of Figure 2(e)]. We use SSM to image $B_z(x, y)$ at 70 nm above the magnet surface at 4.2 K, with B_{ext} applied along y . We note that the stray field significantly exceeds the SQUID monotonic response range of about 100 mT. Thus, we employ a method to extract field values from a modulating SQUID signal, as explained in the SI. Figure 2(a) shows the large B_z at the magnet ends, as expected from the B_{ext} direction. We compare these measurements with EM simulations where polycrystalline magnets with a mean isotropic crystallite size of 40 nm and a corrugated surface with a maximum height variation of 20 nm were assumed, consistent with atomic force microscopy (AFM), X-ray diffraction (XRD), and scanning electron microscopy (SEM) measurements (see SI). We mimic the finite size of the scanning SQUID loop in the simulation by applying a square filter with an edge size of 110 nm. At the poles of the magnets, the simulated and experimentally obtained stray fields are in excellent agreement (SI). The inner two poles provide the stray field suitable for EDSR drive of spin qubits. We notice some small modulation of B_z over the entire magnet structure. To better understand the origin of this, we focus on the regions between the poles of each magnet [framed in Figure 2(a)]. There, B_z fluctuates with a peak-to-peak amplitude of 10 mT [Figure 2(b)], and the overall pattern is inverted if the external field direction is reversed. The amplitude of these modulations decreases with increasing fields, as seen quantitatively from a plot of the standard deviation of the measured field (σ_{B_z}) versus B_{ext} in Figure 2(d).

In Figure 2(d) we compare the SSM experiment with EM simulations. The experimental σ_{B_z} curves show a peak at B_{ext} close to the coercive field (≈ 20 mT). If B_{ext} is increased, then σ_{B_z} monotonically decreases. We can reproduce the experimental data by assuming either a cubic MCA constant of $K_1 = 300$ kJ/m³ and 40 nm crystallite mean size (λ) or $K_1 = 60$ kJ/m³ and $\lambda = 120$ nm (data not shown). For $K_1 = 60$ kJ/m³ and λ

$= 40$ nm, σ_{B_z} initially decreases to a lower level but then monotonically increases from $B_{\text{ext}} = 100$ mT, reaching the same value as in the experiment only at $B_{\text{ext}} = 500$ mT.

We can understand the different trends by inspecting the simulated magnetization direction at different B_{ext} from which we can draw conclusions about the relative size of the Zeeman, MCA, and magnetostatic energies. At $|B_{\text{ext}}| \approx 20$ mT the magnetization state is dominated by local defects and MCA, leading to a peak in σ_{B_z} . At $B_{\text{ext}} = 500$ mT the Zeeman energy dominates and the magnetization is mostly aligned to the direction of the magnetic field, such that surface roughness determines the value of σ_{B_z} (due to the formation of magnetic charges on the corrugated surface). At intermediate fields ($100 < |B_{\text{ext}}| < 380$ mT), the ratio between the MCA and the magnetostatic energy determines the trend of σ_{B_z} with decreasing B_{ext} . For small MCA, the local magnetization progressively orients more parallel to the surface to minimize the amount of magnetic charges along the corrugations, resulting in a decrease of σ_{B_z} . For large MCA, however, the magnetization in each crystallite orients toward the respective easy direction, whereby σ_{B_z} increases.

We now discuss why we need to adapt either λ to 120 nm (three times larger than the measured crystallite size) or K_1 to 300 kJ/m³ (five times larger than the literature value) to match the experimental data. On one hand, the simulation where K_1 is increased could account for the elongated shape of the crystallites (XRD and AFM measurements indicate 15 nm along the smallest and 40 nm along the largest axis; see the SI). The larger K_1 could thus emulate a mixed anisotropy (composed of shape anisotropy and MCA^{21,22}). On the other hand, increasing λ could suggest the formation of so-called "interaction domains".^{23,24} These domains are formed by nanocrystallites that combine together into effective domains with a combined magnetization direction. Indeed, exchange-coupled crystallites with size comparable to the exchange length ($l_{\text{ex}} = \sqrt{2A/(\mu_0 M_{\text{sat}}^2)} \approx 5$ nm, where A is the exchange stiffness constant) cannot vary their magnetization direction abruptly from one crystallite to another.^{25,26} The two possibilities exhibit different correlation lengths of the σ_{B_z} variations, which we, however, cannot distinguish in the experiment because of the finite size of the SQUID loop. We also note that the presence of mixed anisotropy and the formation of interaction domains are not mutually exclusive, such that a combination of both effects may take place.

We now draw our attention to the magnetic field within the gap between the two magnets. Excellent matching between the simulations and the SSM experiment at $B_{\text{ext}} = 100$ mT is found [Figure 2(c)]. The driving gradient dB_z/dy is calculated both for the SSM measurement and for the simulations by fitting the data with a polynomial function and taking its analytical derivative (SI). The comparison between simulation and experiment is shown in Figure 2(e) (additional external fields in SI). We report gradients dB_z/dy larger than 1 mT/nm, currently the largest stray field gradient measured by SSM. The impact of MCA on the driving gradient is small: simulations with different crystallite patterns deviate by less than 5%. We note that the actual gradients experienced by the qubits may be even larger (SI), since the finite size of the SQUID loop (110 nm) is considerably larger than the electron wave function.²⁷ This confirms that Fe micromagnets would provide large and

reproducible driving gradients for the EDSR drive of electron spin qubits.

Despite its smaller saturation magnetization and larger MCA than for Fe, Co is currently the most commonly used material for the fabrication of EDSR magnets.^{8,15,28,29} We now investigate the effect of magnetization pattern relaxation, nanofabrication-related imperfections, and polycrystallinity on the qubit properties in a recent 6-qubit experiment¹⁰ where Co was used as magnetic material. The design [Figure 3(a)] was intended to provide a linear decrease of f_L for six qubits along the x direction, according to calculations made with the MS approximation and assuming perfectly symmetric and sharp edges.¹⁰ Within these approximations, the linear change of f_L is a consequence of the linear variation of the gap size along x . Nevertheless, the experimentally measured f_L show a parabolic dependence on the qubit position along x [Figure 3(c)], which we explain in the following.

Impurity inclusions and surface oxidation degrade the quality of the magnetic material, causing a reduction in the saturation magnetization (see the SI). We expect that for unprotected magnets (like the ones used in ref 10) the saturation magnetization is reduced and we set $M_{\text{sat}} = 1.11$ MA/m to fit the experimental values (23% reduction). Also, nanofabrication patterning may lead to modification of the intended magnet edge profile, as it was the case for this experiment. Thus, we take into account the measured triangular profile in our simulation (see the SI). We then account for MCA by setting a random crystallite pattern with an average size of 40 nm, as extracted from SEM images (SI) and a uniaxial MCA constant of $K_u = 600$ kJ/m³ (the literature value for Co²¹). The resulting magnetization at $B_{\text{ext}} = 380$ mT for one specific crystallite pattern is shown in Figure 3(b), highlighting the magnetization direction modulation.

In Figure 3(c) EM simulations with 10 different crystallite patterns are compared with an EM simulation without MCA, an MS simulation, and the Philips et al. experiment.¹⁰ The random orientation of the different crystallites effectively acts like a reduction of the overall magnetization, thereby also reducing the stray field at the qubit position. In addition, different crystallite patterns spatially modulate the f_L with an amplitude reaching 0.5 GHz [Figure 3(c)]. The overall trend is well captured by the average of the 10 crystallite patterns, but the variations suggest that samples grown under identical conditions will provide stray fields with significantly different profiles. The EM simulation without MCA shows larger fields than the MS simulation, which we explain by the magnetization rotation along the z direction caused by the triangular profile of the magnets.

We now use the simulations to estimate the charge noise displacement δ acting on the qubits, gaining insight into a parameter that is difficult to measure directly. The qubit dephasing rate Γ is linked to δ by $\Gamma = \pi\sqrt{2} \frac{\gamma_e}{h} \left(\frac{dB_z}{dx} + \frac{dB_z}{dy} \right) \delta$ (SI). We plot the dephasing rates ($\Gamma = 1/T_2^*$) experimentally measured¹⁰ in Figure 3(d) and use Δ as the fitting parameter, finding good agreement between the averaged curve and the measured values for a displacement amplitude of $\delta = 28$ pm. This value is comparable with what has been estimated in other SiGe platforms³⁰ but here determined with more confidence. The spread between the different curves is due to the different crystallite patterns that shift the zero crossing of $dB_z/dy(y)$ away from $y = 0$ (where the qubits are located).

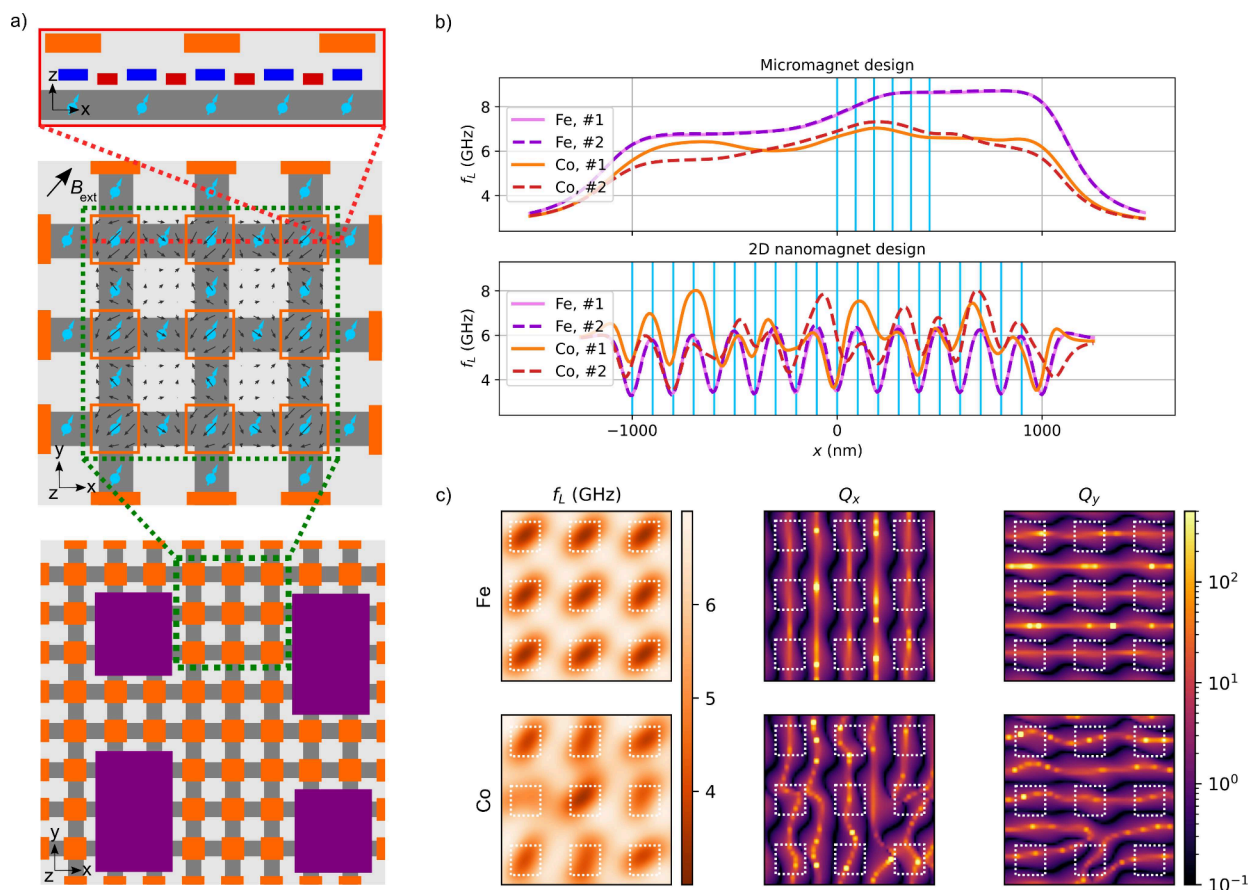


Figure 4. (a) Device geometry showing qubits (blue spins) placed on a two-dimensional grid (hosting structure schematized by dark gray stripes) and nanomagnets (orange). In the cross-sectional view at the top, plunger gates (dark blue) and barrier gates (red) are also shown. Additional structures (such as charge sensing dots, read-out lines, gate vias) can be placed close to the qubit array into gaps of the qubit arrays (violet rectangles, bottom panel). In the middle panel the black arrows show the in-plane components of the magnetic stray field. (b) Comparison of simulated f_L for qubits placed along varying x positions: micromagnet design discussed in Figure 3 (upper panel) and a 11 by 11 nanomagnet array (lower panel), both for Fe and Co and for two different crystallite patterns. The targeted qubit positions are shown as blue vertical lines. (c) Simulated f_L and Q_x and Q_y for Fe and Co nanomagnets. The magnetic field deviations are much larger for Co than for Fe. Nanomagnets are squares with edge length of 50 nm (contours shown as white dotted lines).

This shift is up to 20 nm, about the size of the assumed crystallite dimensions (not shown).

In view of future devices, we note that surface roughness can be controlled by improving fabrication (line edge roughness values of <1 nm are routinely achieved in current semiconductor processing³¹), reducing its impact on the stray field variation. On the other hand, the large MCA of Co combined with polycrystallinity will still have a detrimental effect on qubit properties, randomly altering f_L and increasing dephasing. One way to reduce stray field variations would be to decrease the MCA by switching to different materials, since K_1 varies strongly among ferromagnetic materials and alloys.²¹

We analyze the effect of material choice by simulating the same magnet design for both Fe and Co in Figure 4(b), upper panel. We plot f_L along the x direction at $y = 0$ and $z = -150$ nm. The maximum difference between two stray field profiles with two different crystal patterns for Fe is ≈ 0.05 GHz, 1 order of magnitude smaller than for Co, as already seen for the driving gradient. dots, readout lines, or gate vias²⁷ Ni has an even lower MCA compared to Fe, but its lower $M_{\text{sat}} = 0.49$ MA/m will lead to smaller stray fields and thus smaller driving gradients (see the SI for a more detailed discussion).

After having highlighted the relevant parameters of the magnets that impact EDSR manipulation, we now focus our

attention on a design that is suitable to drive qubits arranged on a 2D lattice. We suggest a 2D Fe nanomagnet architecture, where the magnets are arranged on a square lattice with a period of twice the qubit spacing (Figure 4). Quantum dots hosting the qubits are placed below and between each square magnet, tuned by plunger and barrier gates set in planes below the magnet layer. The magnets either are placed above those gates, providing the electric confinement, or themselves act as a gate^{32–35} by replacing every second plunger gate, further boosting the attainable driving gradient.

We discuss simulation results with $B_{\text{ext}} = 200$ mT applied in a direction tilted 45° with respect to the magnet grid. The magnetic stray field oscillates periodically both in its x and y component, as shown in the middle panel of Figure 4(a). This arrangement has several advantages. First, qubit manipulation can be performed by displacing the wave function both along the x direction and along the y direction (using the neighboring barrier gates). This opens up the possibility to drive qubits arranged on a 2D grid, either by EDSR or by baseband pulsing.³⁶ Second, the magnet arrangement also provides different f_L values for neighboring qubits since the stray field either adds to or subtracts from the external field. The difference between f_L of neighboring qubits is on the order of GHz, substantially larger than the modulation induced

by the MCA [Figure 4(b) and (c)]. Moreover, this design is scalable to any qubit grid size without the need for additional magnetic structures to improve single-qubit addressability, assuming that the electric field used for the EDSR drive of one qubit does not affect the next-nearest neighbor. The geometry is also flexible in terms of how dense the magnet grid can be made locally. Magnets must be placed at the crossing between vertical and horizontal lines of qubits, but the distance between the next line can be any multiple of twice the qubit pitch. Such flexibility opens up possibilities to accommodate additional structures within the grid spanned by the magnets, such as charge sensing dots, readout lines, or gate vias [Figure 4(a), bottom panel].

We have simulated a 11×11 nanomagnet array as squares with an edge length of 50 nm and thickness of 30 nm and plotted the simulation at a height of 45 nm below the lower edge of the magnet. Figure 4(b,c) show that for Fe nanomagnets the stray field pattern repeats with minimal variations along both directions of the magnet array ($\Delta f_L < 50$ MHz). In contrast, for Co nanomagnets, Δf_L may reach up to 2 GHz. These results highlight the different approach between micro- and nanomagnets. For state-of-the-art EDSR-driven qubits, the global field enabling manipulation and single-qubit addressability is modulated by the shape variation of the magnet.^{10,29} There single-qubit EDSR manipulation is performed with a global electric field, meaning that all qubit wave functions are displaced simultaneously. Such an approach forces the requirement that all qubits must have different f_L values to enable single-qubit addressability. This is fulfilled by designing large magnet shape variations with respect to the qubit dimensions, maximizing the driving gradient while keeping the required minimal Δf_L between the qubits (see the SI). Figure 4(b) also compares two different crystallite structures, showing that the MCA in Co may strongly modulate the stray field and lift the engineered f_L differences.

In our architecture, the stray field direction rotates on a length scale commensurate with the qubit pitch. Errors in fabrication and alignment are of similar relevance to those for micromagnets (which can be mitigated by improving fabrication), but MCA-induced variations are negligible if the magnets are made of Fe. We also note that the large variation in stray field between neighboring qubits can be advantageous for spin shuttling,³⁷ thanks to an effective dynamical decoupling during the transfer. The resilience toward stray field variations is also visible in the quality factor plots of Q_x and Q_y [Figure 4(c)]. We define $Q_i = \frac{dB_z/di}{dB_{\parallel}/di}$, with $i \in (x, y)$, since the qubits have to be displaced either along the x or the y direction depending on their location between the magnets. B_{\parallel} is the magnetic field along the qubit quantization axis. In the Fe simulation, the zero crossing of the dephasing gradient persistently coincides with the maxima or minima of the driving gradient along either the x or y direction, such that $Q_i > 30$ is expected at the foreseen qubit locations.

In conclusion, we have shown that micromagnetic simulations enabled us to accurately model and quantify the impact of sample polycrystallinity, MCA, and fabrication-related imperfections on the magnetic stray field. We compared our simulations with SSM measurements at different external magnetic fields and with experimentally determined spin qubit properties, finding good agreement. Corroborated by these findings, we propose to use Fe as the magnetic material for EDSR magnets because of its higher saturation

magnetization and lower MCA than Co. Furthermore, we have developed a qubit architecture with Fe magnets, which enables driving qubits on a two-dimensional grid. Our architecture is locally tunable in sparsity and achieves quality factors above 30 with low next-neighbor crosstalk. In addition to demonstrating the importance of micromagnetic simulations to accurately model the performance of nanomagnets for spin qubits, these findings provide a means for designing future architectures for nanomagnet-based spin qubit manipulation.

■ ASSOCIATED CONTENT

Data Availability Statement

All data underlying this study are available at Zenodo at <https://zenodo.org/records/14650693>.

Supporting Information

The Supporting Information is available free of charge at <https://pubs.acs.org/doi/10.1021/acs.nanolett.4c05037>.

Details on micromagnetic simulations, additional magnet designs and magnetic material choice; details of SSM measurement and calibration; AFM, SEM, and XRD characterization; vibrating sample magnetometry; additional references (PDF)

■ AUTHOR INFORMATION

Corresponding Author

Gian Salis – IBM Research—Zurich, 8803 Rüschlikon, Switzerland; Email: gsa@zurich.ibm.com

Authors

Michele Aldeghi – IBM Research—Zurich, 8803 Rüschlikon, Switzerland; orcid.org/0000-0001-6883-6179

Rolf Allenspach – IBM Research—Zurich, 8803 Rüschlikon, Switzerland

Andriani Vervelaki – Department of Physics, University of Basel, 4056 Basel, Switzerland

Daniel Jetter – Department of Physics, University of Basel, 4056 Basel, Switzerland

Kousik Bagani – Department of Physics, University of Basel, 4056 Basel, Switzerland

Floris Braakman – Department of Physics, University of Basel, 4056 Basel, Switzerland

Martino Poggio – Department of Physics, University of Basel, 4056 Basel, Switzerland; Swiss Nanoscience Institute, University of Basel, 4056 Basel, Switzerland; orcid.org/0000-0002-5327-051X

Complete contact information is available at:

<https://pubs.acs.org/10.1021/acs.nanolett.4c05037>

Notes

The authors declare no competing financial interest.

■ ACKNOWLEDGMENTS

We thank the Cleanroom Operations Team of the Binnig and Rohrer Nanotechnology Center (BRNC) for advice and support on sample fabrication. We thank Armin Knoll for his support with AFM measurements and Thomas Weber and Marilyne Sousa for their help with XRD measurements. We gratefully acknowledge Brennan Undseth, Lieven Vandersypen, and all members of the Spin Qubit team at IBM and of the Poggio Lab for fruitful discussions. This work was supported as a part of the NCCR SPIN project funded by the Swiss National Science Foundation (grant number 51NF40-

180604). We also acknowledge support by the European Commission under H2020 FET Open grant “FIBSuperProbes” (Grant No. 892427) and the Swiss National Science Foundation under Grant No. 200020-207933.

REFERENCES

- (1) INSIC International Magnetic Tape Storage Technology Roadmap 2024. 2024; <https://insic.org/wp-content/uploads/2024/08/INSIC-International-Magnetic-Tape-Storage-Technology-Roadmap-2024-1.pdf>, Accessed: 2024-09-18.
- (2) Tuma, T.; Pantazi, A.; Sahoo, D. R.; Eib, P.; Salis, G.; Pozidis, H.; Sebastian, A. A high-bandwidth spintronic position sensor. *Nanotechnology* **2014**, *25*, 375501.
- (3) Skjærø, S. H.; Marrows, C. H.; Stamps, R. L.; Heyderman, L. J. Advances in artificial spin ice. *Nature Review Physics* **2020**, *2*, 13–28.
- (4) Marchiori, E.; Ceccarelli, L.; Rossi, N.; Lorenzelli, L.; Degen, C. L.; Poggio, M. Nanoscale magnetic field imaging for 2D materials. *Nature Review Physics* **2022**, *4*, 49–60.
- (5) Loss, D.; DiVincenzo, D. P. Quantum computation with quantum dots. *Phys. Rev. A* **1998**, *57*, 120–126.
- (6) Allenspach, R.; Salis, G. R. *Method of manipulating a quantum system comprising a magnetic moment*, Patent US7336515, 2008.
- (7) Tokura, Y.; van der Wiel, W. G.; Obata, T.; Tarucha, S. Coherent single electron spin control in a slanting Zeeman field. *Phys. Rev. Lett.* **2006**, *96*, 047202.
- (8) Pioro-Ladrière, M.; Obata, T.; Tokura, Y.; Shin, Y. S.; Kubo, T.; Yoshida, K.; Taniyama, T.; Tarucha, S. Electrically driven single-electron spin resonance in a slanting Zeeman field. *Nat. Phys.* **2008**, *4*, 776–779.
- (9) Yoneda, J.; Takeda, K.; Otsuka, T.; Nakajima, T.; Delbecq, M. R.; Allison, G.; Honda, T.; Kodera, T.; Oda, S.; Hoshi, Y.; Usami, N.; Itoh, K. M.; Tarucha, S. A quantum-dot spin qubit with coherence limited by charge noise and fidelity higher than 99.9. *Nat. Nanotechnol.* **2018**, *13*, 102–106.
- (10) Philips, S. G.; Madzik, M. T.; Amitonov, S. V.; de Snoo, S. L.; Russ, M.; Kalhor, N.; Volk, C.; Lawrie, W. I.; Brousse, D.; Tryputen, L.; Wuetz, B. P.; Sammak, A.; Veldhorst, M.; Scappucci, G.; Vandersypen, L. M. Universal control of a six-qubit quantum processor in silicon. *Nature* **2022**, *4*, 919–924.
- (11) Noiri, A.; Takeda, K.; Nakajima, T.; Kobayashi, T.; Sammak, A.; Scappucci, G.; Tarucha, S. Fast universal quantum gate above the fault-tolerance threshold in silicon. *Nature* **2022**, *601*, 338–342.
- (12) Xue, X.; Russ, M.; Samkharadze, N.; Undseth, B.; Sammak, A.; Scappucci, G.; Vandersypen, L. M. Quantum logic with spin qubits crossing the surface code threshold. *Nature* **2022**, *601*, 343.
- (13) Mills, A. R.; Guinn, C. R.; Gullans, M. J.; Sigillito, A. J.; Feldman, M. M.; Nielsen, E.; Petta, J. R. Two-qubit silicon quantum processor with operation fidelity exceeding 99. *Science Advances* **2022**, *8*, 5130.
- (14) Yoneda, J.; Otsuka, T.; Takakura, T.; Pioro-Ladrière, M.; Brunner, R.; Lu, H.; Nakajima, T.; Obata, T.; Noiri, A.; Palmstrøm, C. J.; Gossard, A. C.; Tarucha, S. Robust micromagnet design for fast electrical manipulations of single spins in quantum dots. *Applied Physics Express* **2015**, *8*, 084401.
- (15) Struck, T.; Hollmann, A.; Schauer, F.; Fedorets, O.; Schmidbauer, A.; Sawano, K.; Riemann, H.; Abrosimov, N. V.; Cywiński, Ł.; Bougeard, D.; Schreiber, L. R. Low-frequency spin qubit energy splitting noise in highly purified 28Si/SiGe. *npj Quantum Information* **2020**, *6*, 1–7.
- (16) Neumann, R.; Schreiber, L. Simulation of micro-magnet stray-field dynamics for spin qubit manipulation. *J. Appl. Phys.* **2015**, *117*, 193903.
- (17) Wyss, M.; Bagani, K.; Jetter, D.; Marchiori, E.; Vervelaki, A.; Gross, B.; Ridderbos, J.; Gliga, S.; Schönenberger, C.; Poggio, M. Magnetic, thermal, and topographic imaging with a nanometer-scale SQUID-on-lever scanning probe. *Physical Review Applied* **2022**, *17*, 034002.
- (18) Miltat, J. E.; Donahue, M. J. In *Handbook of Magnetism and Advanced Magnetic Materials*; Kronmüller, H., Parkin, S., Eds.; Wiley, 2007; Vol. 2; Chapter Numerical Micromagnetics: Finite Difference Methods.
- (19) Brunner, R.; Shin, Y.-S.; Obata, T.; Pioro-Ladrière, M.; Kubo, T.; Yoshida, K.; Taniyama, T.; Tokura, Y.; Tarucha, S. Two-Qubit Gate of Combined Single-Spin Rotation and Interdot Spin Exchange in a Double Quantum Dot. *Phys. Rev. Lett.* **2011**, *107*, 146801.
- (20) Meyer, E.; Hug, H. J.; Bennowitz, R. *Scanning Probe Microscopy: the Lab on a Tip*; Springer, 2004.
- (21) Cullity, B. D.; Graham, C. D. *Introduction to Magnetic Materials*; John Wiley & Sons, 2011.
- (22) Nesbitt, E.; Williams, H.; Bozorth, R. M. Factors determining the permanent magnet properties of single crystals of Fe₂NiAl. *J. Appl. Phys.* **1954**, *25*, 1014–1020.
- (23) Craik, D.; Isaac, E. Magnetic interaction domains. *Proceedings of the Physical Society* **1960**, *76*, 160.
- (24) Hadjipanayis, G. C. Nanophase hard magnets. *J. Magn. Magn. Mater.* **1999**, *200*, 373–391.
- (25) Goll, D. In *Handbook of Magnetism and Advanced Magnetic Materials*; Kronmüller, H., Parkin, S., Eds.; Wiley, 2007; Vol. 2; Chapter Micromagnetism – Microstructure relations and the hysteresis loop.
- (26) Schäfer, R.; Hubert, A.; Herzer, G. Domain observation on nanocrystalline material. *J. Appl. Phys.* **1991**, *69*, 5325–5327.
- (27) Aldeghi, M.; Allenspach, R.; Salis, G. Modular nanomagnet design for spin qubits confined in a linear chain. *Appl. Phys. Lett.* **2023**, *122*, 134003.
- (28) Watson, T. F.; Philips, S. G.; Kawakami, E.; Ward, D. R.; Scarlino, P.; Veldhorst, M.; Savage, D. E.; Lagally, M. G.; Friesen, M.; Coppersmith, S. N.; Eriksson, M. A.; Vandersypen, L. M. A programmable two-qubit quantum processor in silicon. *Nature* **2018**, *555*, 633–637.
- (29) Yoneda, J.; Rojas-Arias, J.; Stano, P.; Takeda, K.; Noiri, A.; Nakajima, T.; Loss, D.; Tarucha, S. Noise-correlation spectrum for a pair of spin qubits in silicon. *Nat. Phys.* **2023**, *19*, 1793–1798.
- (30) Kawakami, E.; Scarlino, P.; Ward, D. R.; Braakman, F. R.; Savage, D. E.; Lagally, M. G.; Friesen, M.; Coppersmith, S. N.; Eriksson, M. A.; Vandersypen, L. M. Electrical control of a long-lived spin qubit in a Si/SiGe quantum dot. *Nat. Nanotechnol.* **2014**, *9*, 666–670.
- (31) IEEE Line Edge Roughness White Paper for the International Roadmap on Devices and Systems. 2021; <https://irds.ieee.org/images/files/pdf/2021/LER-white-paper.pdf>, Accessed: 2024-09-18.
- (32) Forster, F.; Mühlbacher, M.; Schuh, D.; Wegscheider, W.; Ludwig, S. Electric-dipole-induced spin resonance in a lateral double quantum dot incorporating two single-domain nanomagnets. *Phys. Rev. B* **2015**, *91*, 195417.
- (33) Bersano, F.; Aldeghi, M.; Collette, E.; Ghini, M.; De Palma, F.; Oppliger, F.; Scarlino, P.; Braakman, F.; Poggio, M.; Riel, H.; Salis, G.; Allenspach, R.; Ionescu, A. M. Quantum Dots Array on Ultra-Thin SOI Nanowires with Ferromagnetic Cobalt Barrier Gates for Enhanced Spin Qubit Control. *2023 IEEE Symposium on VLSI Technology and Circuits (VLSI Technology and Circuits)*; 2023; pp 1–2.
- (34) Tadokoro, M.; Nakajima, T.; Kobayashi, T.; Takeda, K.; Noiri, A.; Tomari, K.; Yoneda, J.; Tarucha, S.; Kodera, T. Designs for a two-dimensional Si quantum dot array with spin qubit addressability. *Sci. Rep.* **2021**, *11*, 19406.
- (35) Simion, G. E.; Mohiyaddin, F. A.; Kubicek, S.; Govoreanu, B.; Ciubotaru, F.; Ruoyu, L. *Qubit device and a method for operating a qubit device*. 2024; Patent US12027610.
- (36) Wang, C.-A.; et al. Operating semiconductor quantum processors with hopping spins. *Science* **2024**, *385*, 447–452.
- (37) Bosco, S.; Zou, J.; Loss, D. High-Fidelity Spin Qubit Shuttling via Large Spin-Orbit Interactions. *PRX Quantum* **2024**, *5*, 020353.